Supporting Information

Enhanced Directional Fluorescence Emission of Randomly Oriented Emitters via Metal-Dielectric Hybrid Nanoantenna

Song Sun[1,2], Taiping Zhang[1,2], Qing Liu[3], Li Ma[1,2], Qingguo Du[4,5], Huigao Duan[3]*

[1]*Microsystem & Terahertz Research Center, China Academy of Engineering Physics, No.596, Yinhe Road, Shuangliu, Chengdu, China 610200.*

[2]*Insititute of Electronic Engineering, China Academy of Engineering Physics, Mianyang, China 621999.*

[3]*State-Key Laboratory of Advanced Design and Manufacturing of Vehicle Body, Colledge of Mechanical and Vehicle Engineering, Hunan University, Changsha, China 410082.*

[4]*School of Information Engineering, Wuhan University of Technology, 122 Luo Shi Road, Wuhan, Hubei, China 430070.*

[5]*Hubei Key Laboratory of Broadband Wireless Communication and Sensor Networks (Wuhan University of Technology), Wuhan, Hubei, China 430070.*

*Corresponding author, Email: sunsong@mtrc.ac.cn

1. Omnidirectional far field radiation of randomly oriented emitters in free space

Figure S1 illustrates the overall far field radiation pattern of randomly oriented emitters in the free space. The emitters are uniformly distributed in the identical space as those for the hybrid nanoantenna. As expected, an omnidirectional radiation is observed hence verifying the fidelity of the reciprocity principle. This value is also used as the reference in the normalization process in Figure 9 in the main text.

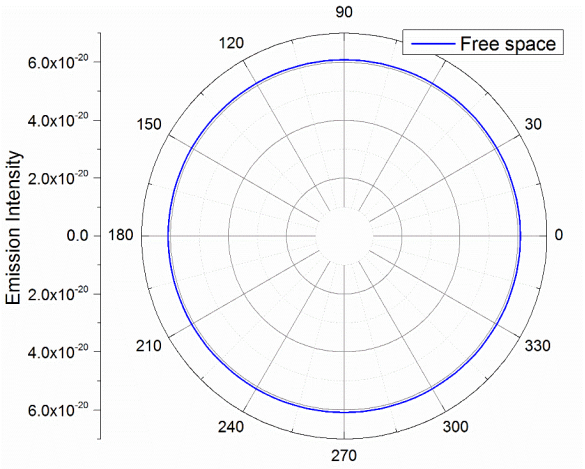

Figure S1. Omnidirectional far field radiation patterns of randomly oriented emitters in free space.

2. Finite element modelling

The scattering wave formulation in the frequency domain solver is adopted in the finite element modelling. The main computation domain is 2λ, where λ is the wavelength, and the perfect matching layers (PML) with thickness $\lambda/2$ are used to absorb any unphysical reflection at the domain boundary. The scattering power is computed via the surface integration of the power outflow from a spherical surface surrounding the nanoantenna, and the loss is obtained via the volume integration of the power dissipated inside the nanoantenna. During the excitation process,

the background input field is set to be the vertically incident plane wave, and the excitation rate can be retrieved at any domain point. During the emission process, the background input field is set to null, and a point dipole source is added in the gap region. For the reciprocity calculation, three frequency domain steps are adopted in a single simulation. The first is the plane wave incidence propagates vertically to account the excitation process, the second and third are used to compute the optical response under *S*- and *P*-polarized plane wave oblique incidences from certain angle (θ, φ). The emission intensity can thus be obtained with the solutions from the three steps using Eq. (8) and (9). The mesh size is 8 nm for the Au nanodisk and the gap region, 20 nm for the Si ring, and $\lambda/5$ for the surrounding environment.

3. Stable plasmonic resonance in isolated Au nanodisk

The geometrical effect of the isolated Au nanodisk on its plasmonic resonance is shown in Figure S2. The variation in the radius R_m or height H of the Au nanodisk mainly affects the magnitude of the extinction cross-section (CS), whereas they only induces a minor change in the spectral position of the plasmonic resonance peak ($\Delta\lambda < 10$ nm).

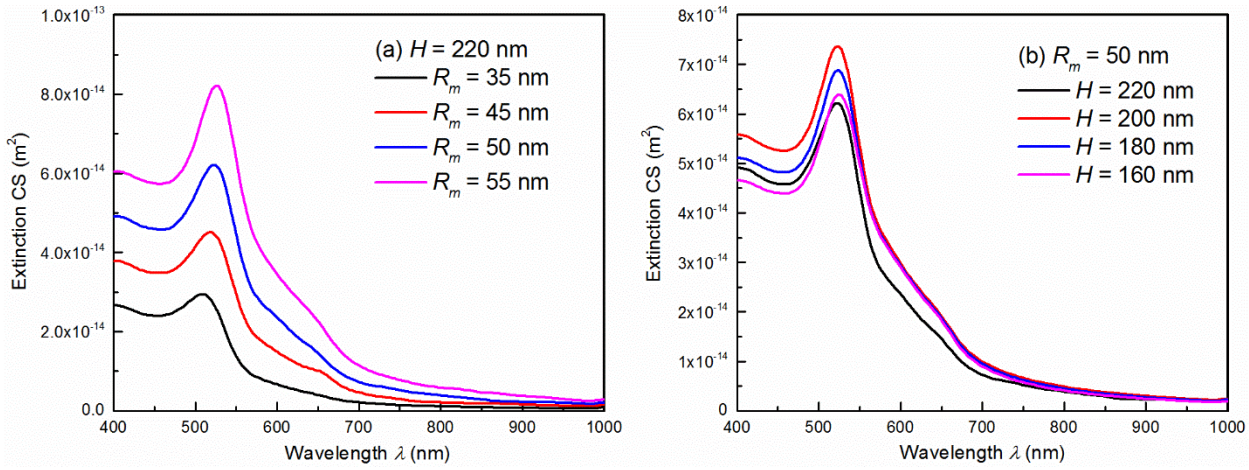

Figure S2. Extinction cross-sections of isolated Au nanodisk with various radius R_m and height H. Spectral position of plasmonic resonances remains stable upon variation of Au nanodisk geometry.

4. Flexible tunability of electric and magnetic resonances in isolated Si nano-ring

Figure S3 illustrates the changes in the extinction spectra of the isolated Si nano-ring with respect to the variations in the geometrical parameters: the inner radius R_{in}, the outer radius R_{out} and the height H. Unlike the isolated Au nanodisk scenario, the geometry of the nano-ring significantly affects the magnitudes and the spectral positions of the dielectric resonances, including both the electric dipole mode (ED) and magnetic dipole mode (MD). Therefore, the Si nano-ring structure offers flexible tunability ($\Delta\lambda$ > 100 nm) to adjust the spectral position of dielectric ED/MD to match the plasmonic resonance of the Au nanodisk, which is critical in analyzing the interference effect between different modes in the hybrid configuration.

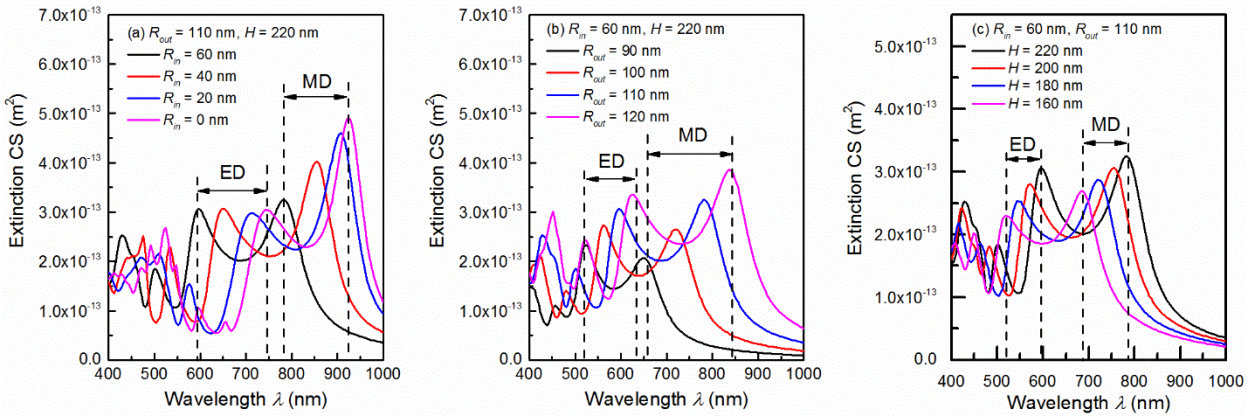

Figure S3. Extinction cross-sections of isolated Si nano-ring with various inner radius R_{in}, outer radius R_{out}, and height H. Nano-ring structure offers excellent tunability to match dielectric ED/MD with plasmonic resonance of Au nanodisk.

5. Vector electric field distribution of Au SPR and Si ring MD

Figure S4 illustrates the vector electric field distributions of the Si ring MD and Au nanodisk SPR at the wavelength 530 nm. It is clear that the dielectric MD yields a rotational electric field inside the central cavity region, and the metal SPR shows a typical electric dipolar pattern. According to the charge distributions inferred from the vector electric field distributions,

a strong attractive force would be established between the two constituents in the gap region when the metal nanodisk is placed inside the dielectric ring cavity. Consequently, such an attractive force would create a strong electric field enhancement in the gap region, which explains the results in Figure 2 in the main text.

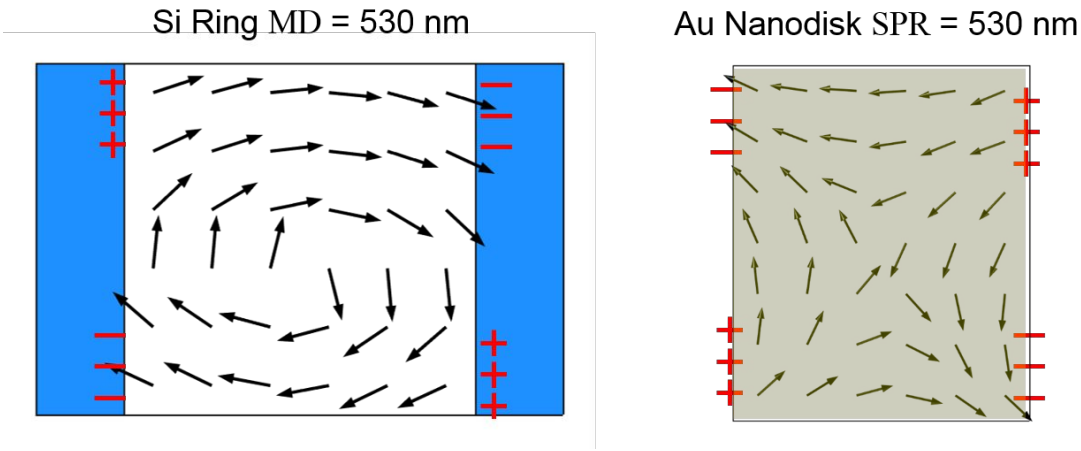

Figure S4. Schematics of vector electric field distributions of Si ring MD and Au nanodisk SPR.

6. Vector electric field distribution of Au SPR and Si ring ED

Figure S5 depicts the vector electric field distributions of the Si ring ED and Au nanodisk SPR at the wavelength 520 nm. In this case, the dielectric ED shows a straight electric dipolar distribution in the central cavity region, which is different from the rotational field distribution pattern for the MD case (see Figure S4). According to the charge distributions at the boundaries, an attractive force arises at the top part of the gap region, whereas a repulsive force occurs at the bottom part when the Au nanodisk is placed inside the Si ring cavity. The attractive and repulsive forces work together and cause a spectral split in the extinction CS, which explains the results in Figure 3 in the main text.

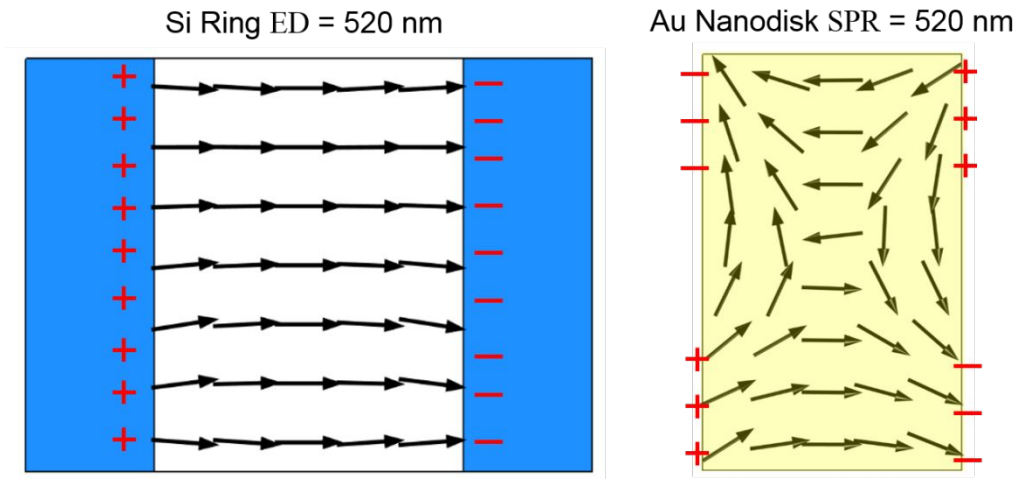

Figure S5. Schematics of vector electric field distributions of Si ring ED and Au nanodisk SPR.

7. Spectral split due to SPR-ED hybridization

Figure S6 shows another case of the SPR-ED hybrid nanoantenna, which consists of a R_m = 50 nm, H = 220 nm Au nanodisk and a R_{in} = 60 nm, R_{out} = 90 nm, H = 220 nm Si ring cavity. The SPR and dielectric ED are aligned at 525 nm. A clearer split is observed in the spectrum due to the SPR-ED interaction.

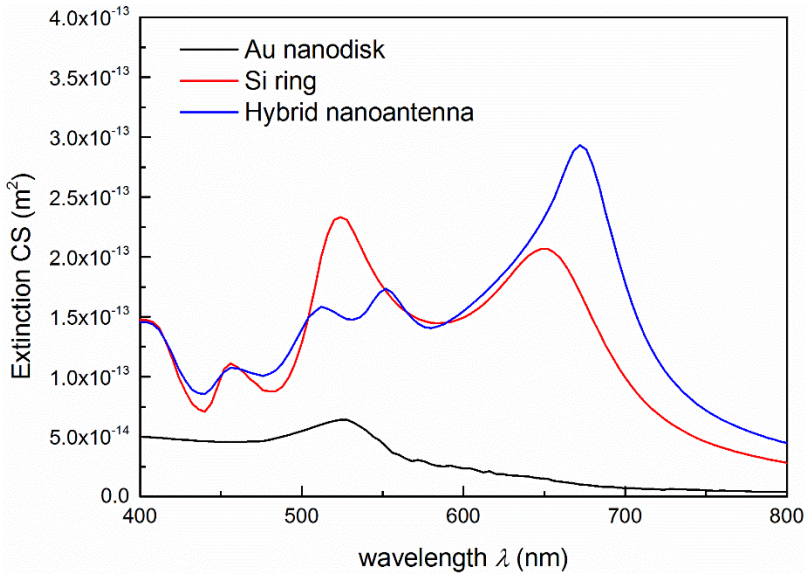

Figure S6. Schematics of electric field distributions of Si ring ED and Au nanodisk SPR.

8. Derivation for coupled oscillator model

The overall equations of motions of the coupled oscillator model are

$$\begin{cases} \ddot{x}_{SPR}(t) + \gamma_{SPR}\dot{x}_{SPR}(t) + w_{SPR}^2 x_{SPR}(t) + g_1\dot{x}_{ED}(t) + g_2\dot{x}_{MD}(t) = F_{SPR}(t) \\ \ddot{x}_{ED}(t) + \gamma_{ED}\dot{x}_{ED}(t) + w_{ED}^2 x_{ED}(t) - g_1\dot{x}_{SPR}(t) + g_3\dot{x}_{MD}(t) = F_{ED}(t) \\ \ddot{x}_{MD}(t) + \gamma_{MD}\dot{x}_{MD}(t) + w_{MD}^2 x_{MD}(t) - g_2 x_{SPR}(t) - g_3\dot{x}_{ED}(t) = F_{MD}(t) \end{cases} \quad \text{(S1)}$$

where $g_3 \approx 0$ is assumed since the internal interactions between multipole modes in the dielectric nanoparticle is neglected in our case. Transform Eq. (S1) into frequency domain, we obtain

$$\begin{cases} -w^2 x_{SPR}(w) + jw\gamma_{SPR}x_{SPR}(w) + w_{SPR}^2 x_{SPR}(w) + jwg_1 x_{ED}(w) + jwg_2 x_{ED}(w) = F_{SPR}(w) \\ -w^2 x_{ED}(w) + jw\gamma_{ED}x_{ED}(w) + w_{ED}^2 x_{ED}(w) - jwg_1 x_{SPR}(w) = F_{ED}(w) \\ -w^2 x_{MD}(w) + jw\gamma_{MD}x_{MD}(w) + w_{MD}^2 x_{MD}(w) - jwg_2 x_{SPR}(w) = F_{MD}(w) \end{cases} \quad \text{(S2)}$$

After some linear algebra, we have

$$x_{SPR}(w) = \frac{k_{ED}k_{MD}F_{SPR}(w) - jwg_1k_{MD}F_{ED}(w) - jwg_2k_{ED}F_{MD}(w)}{k_{SPR}k_{ED}k_{MD} - k_{MD}w^2g_1^2 - k_{ED}w^2g_2^2}$$

$$x_{ED}(w) = \frac{jwg_1x_{SPR}(w) + F_{ED}(w)}{k_{ED}} \quad \text{(S3)}$$

$$x_{MD}(w) = \frac{jwg_2x_{SPR}(w) + F_{MD}(w)}{k_{MD}}$$

where $k_{SPR} = -w^2 + jw\gamma_{SPR} + w_{SPR}^2$, $k_{ED} = -w^2 + jw\gamma_{ED} + w_{ED}^2$, $k_{MD} = -w^2 + jw\gamma_{MD} + w_{MD}^2$, respectively. We note that the driving forces are all in the harmonic forms, e.g. $F_{SPR}(t) = F_{SPR}\, e^{-jw_0t}$, $F_{ED}(t) = F_{ED}e^{-jw_0t}$ and $F_{MD}(t) = F_{MD}e^{-jw_0t}$. In frequency domain $F_{SPR}(w) = \frac{1}{2}F_{SPR}$ $(\delta(w + w_0) + \delta(w - w_0))$, by taking the inverse Fourier transform, we have,

$$x_{SPR}(t) = Re\left[\frac{k_{ED}k_{MD}F_{SPR}(t) - jwg_1k_{MD}F_{ED}(t) - jwg_2k_{ED}F_{MD}(t)}{k_{SPR}k_{ED}k_{MD} - k_{MD}w^2g_1^2 - k_{ED}w^2g_2^2}\right]$$

$$x_{ED}(t) = Re\left[\frac{jwg_1x_{SPR}(t) + F_{ED}(t)}{k_{ED}}\right] \quad \text{(S4)}$$

$$x_{MD}(t) = Re\left[\frac{jwg_2x_{SPR}(t) + F_{MD}(t)}{k_{MD}}\right]$$

where "*Re*" stands for the real part of the complex value.

The resultant extinction cross-section of the system can be seen equivalently as the work done by the external force as $C_{ext}(w) \propto \langle F_{SPR}(t)\dot{x_{SPR}}(t) + F_{ED}(t)\dot{x_{ED}}(t) + F_{MD}(t)\dot{x_{MD}}(t)\rangle = \langle F_{SPR}(t)\dot{x_{SPR}}(t)\rangle + \langle F_{ED}(t)\dot{x_{ED}}(t)\rangle + \langle F_{MD}(t)\dot{x_{MD}}(t)\rangle$, where the bracket represents the averaging over an oscillation period. Straightforwardly, we can obtain the final expressions as,

$$\langle F_{SPR}(t)\dot{x_{SPR}}(t)\rangle = \frac{1}{2}F_{SPR}wIm\left[\frac{k_{ED}k_{MD}F_{SPR} - jwg_1k_{MD}F_{ED} - jwg_2k_{ED}F_{MD}}{k_{SPR}k_{ED}k_{MD} - k_{MD}w^2g_1^2 - k_{ED}w^2g_2^2}\right]$$

$$\langle F_{ED}(t)\dot{x_{ED}}(t)\rangle = \frac{1}{2}F_{ED}wIm\left[\frac{jwg_1x_{SPR} + F_{ED}}{k_{ED}}\right] \quad \text{(S5)}$$

$$\langle F_{MD}(t)\dot{x_{MD}}(t)\rangle = \frac{1}{2}F_{MD}wIm\left[\frac{jwg_2x_{SPR} + F_{MD}}{k_{MD}}\right]$$

where "*Im*" stands for the imaginary part of the complex value.

9. Extinction CS for other incident directions

Compared with the extinction spectra in Figure 2 in the main text, where the incident plane wave propagates vertically, Figure S7 shows the extinction CS of the hybrid nanoantenna where the incident plane wave propagates horizontally. Different modes appear depending on the electric field polarizations. In particular in Figure S7(b), two peaks arise at 490 nm and 700 nm which are consistent with the radiative decay rate spectra of the dipole radiation in Figure 6 in the main text. The radiation of a dipole emitter can be treated as the summation of a group of coherent plane waves with different propagation directions and polarizations. Therefore, the interaction between the dipole emission and the nanoantenna is also the assembly effect of the plane wave incidences with different incident directions and polarizations. This explains why the resonant modes in the dipole radiative decay rate spectra are not the same as that in the plane wave excitation spectra.

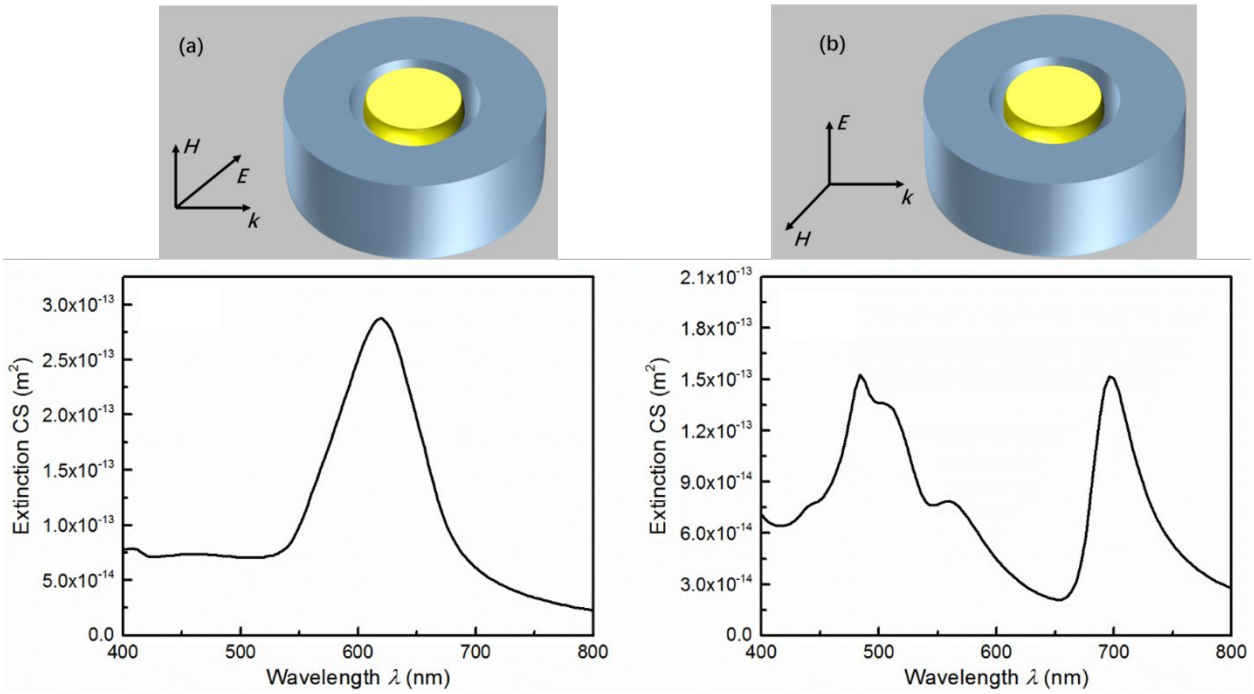

Figure S7. Extinction CS of the hybrid nanoantenna where the incident plane wave propagates horizontally with two different polarizations.

10. Evolution of angular radiation pattern

Figure S8 shows the angular radiation pattern of the hybrid nanoantenna at various wavelengths. The maximum emission intensity occurs at 600 nm, associated with an excellent directivity. The maximum directivity enhancement (e.g. θ = 0) can reach more than 3000 compared to that in the free space. As the wavelength move away from the resonant condition, the emission intensity decreases and the directivity resembles the omnidirectional radiation pattern in the free space.

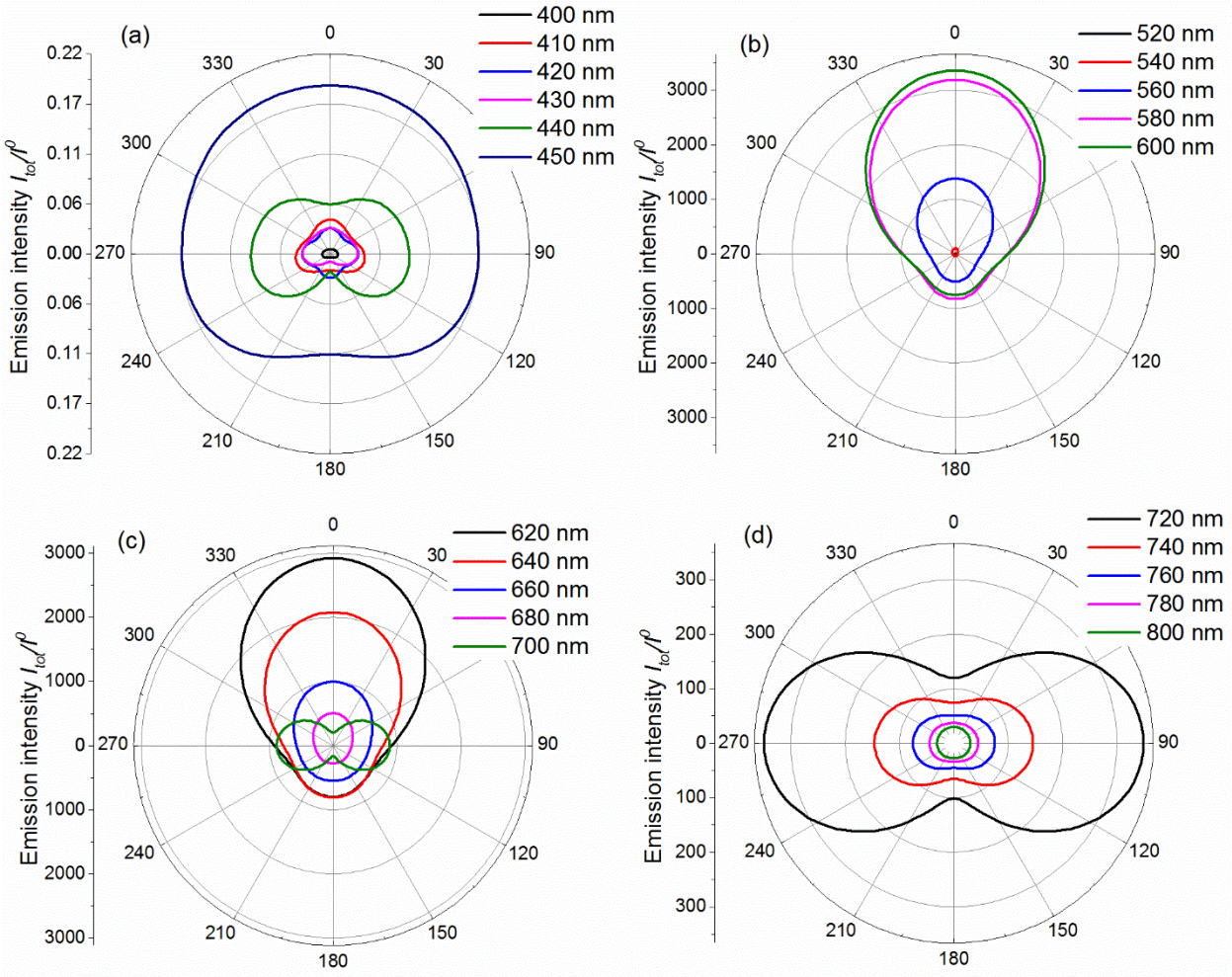

Figure S8. Angular radiation patterns of hybrid nanoantenna at various wavelengths.

11. Angular radiation pattern for pure metal and dielectric nanocomponents

The angular radiation patterns for the pure metal nanodisk and dielectric ring at 600 nm are shown in Figure S9. Although there are some slight modifications on the radiation patterns, the emission directivities are not very good for the pure metal and dielectric components. Only the hybrid nanoantenna can yield an excellent directivity. Note that the emission intensities of the

pure metal and dielectric components are orders of magnitudes smaller than that of the hybrid structure, hence cannot be directly observed in Figure 9 in the main text.

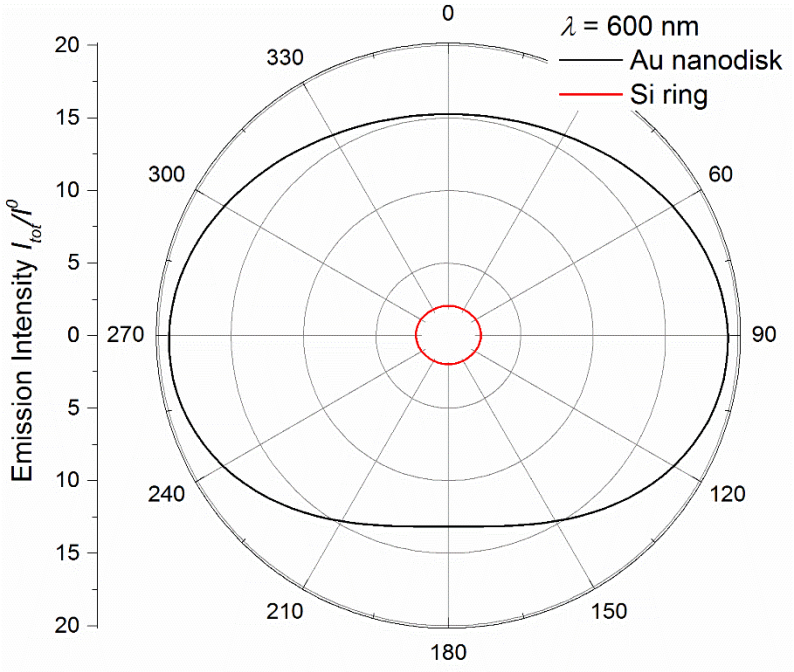

Figure S9. Angular radiation patterns for pure metal nanodisk and dielectric ring at 600 nm.

12. Angular radiation pattern with and without excitation rate

Figure S10 compares the angular radiation pattern of the hybrid nanoantenna for (a) without the excitation rates and (b) with excitation rates. The results show that the effect of the non-uniformly distributed excitation rates not only dramatically increase the magnitudes of the emissions, but also leads to an unsymmetrical directional radiation pattern.

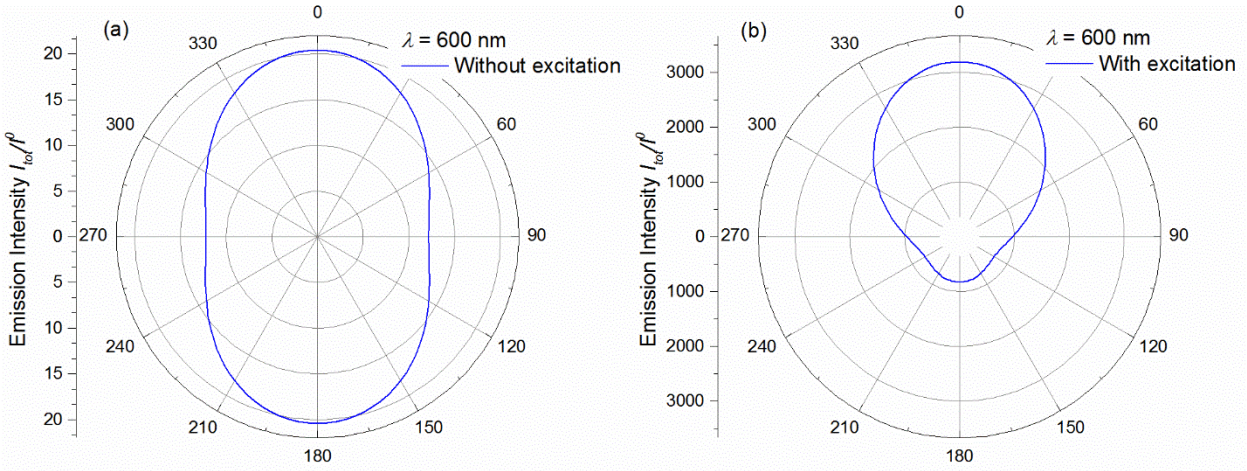

Figure S10. Angular radiation patterns for hybrid nanoantenna at 600 nm for (a) without excitation rate and (b) with excitation rates.

13. Angular radiation pattern of a single emitter

Figure S11 illustrates the far field radiation pattern for a single emitter located at the top part of the antenna gap. Clearly, *x*-oriented emitter shows largest far field intensity and the majority of the radiation power propagates upwards, which will be reflected in the overall angular radiation pattern of multiple randomly oriented emitters. Note that although *z*-oriented emitter also yields a directional pattern with most of emission power propagates upwardly, its magnitude is much lower than that from the *x*-oriented emitter.

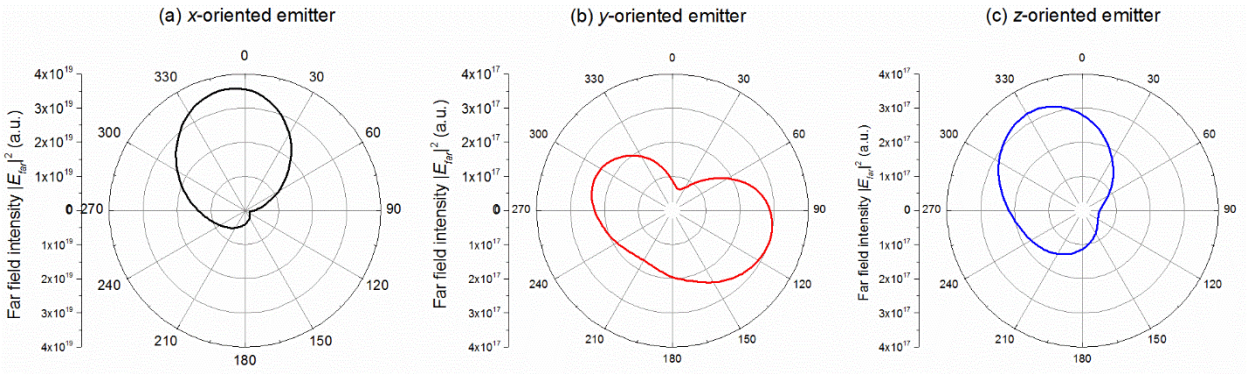

Figure S11. Angular radiation patterns at 600 nm for a single emitter located at top part of antenna gap: (a) *x*-oriented emitter, (b) *y*-oriented emitter and (c) *z*-oriented emitter.

14. Detail data for a different gap size

Since the SPR of the Au nanodisk is invariable to the geometrical alternation (Figure S2), the gap size of the hybrid nanoantenna can be simply controlled by changing the radius of the Au nanodisk. Figure S12(a) shows the extinction spectra of the hybrid nanoantenna with a larger gap size = 20 nm. It is found that a larger gap size substantially reduces the coupling strength between the metal SPR and dielectric MD, leading to a minor red-shifted peak at 550 nm compared to that at 580 nm with a 10 nm gap (see Figure S12(b)). The results of the near field distributions at the SPR-MD hybrid resonant peaks further prove this point as shown in Figure S12(c). A larger gap size yields a smaller near field enhancement in the gap region, compared to that with a smaller gap size.

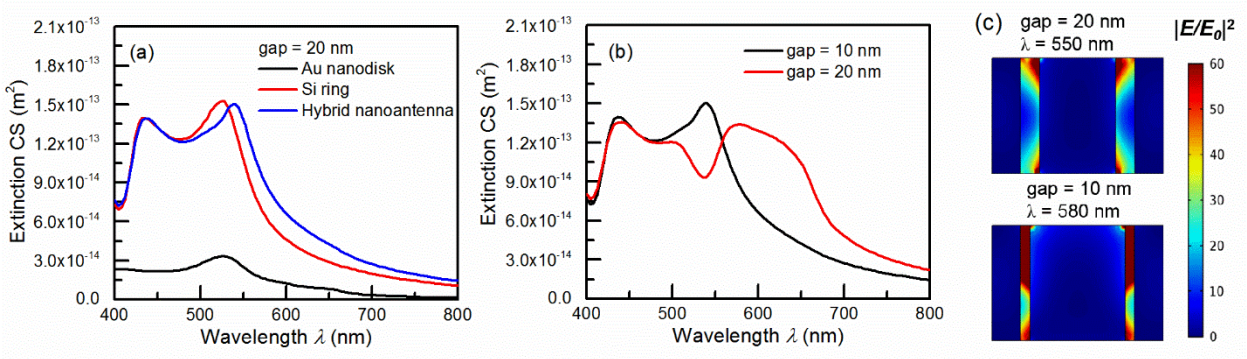

Figure S12. Extinction spectra of hybrid nanoantenna with 20 nm gap compared to (a) pure metal and dielectric component and (b) that with 10 nm gap. (c) Field distributions at SPR-MD hybrid resonant peaks for 10 nm and 20 nm gap respectively.

Assuming the emitter is located at the center of the gap region, the excitation rates of the hybrid nanoantennas with different gap sizes are shown in Figure S13. The excitation rates associated with the 20 nm gap are much smaller than those with a 10 nm gap, which are consistent with the near field distributions in Figure S12. Note that the rapid decrements on the excitation rates can be attributed to two reasons: 1) the coupling strength between SPR and MD decreases; and 2) the emitter is located at a larger distance ~ 10 nm from the surface of either metal or dielectric constituent at gap = 20 nm, whereas it is ~ 5 nm from the antenna surface at gap = 10 nm. Due to evanescent nature of the near field in the gap region, a larger distance means a smaller electric field enhancement.

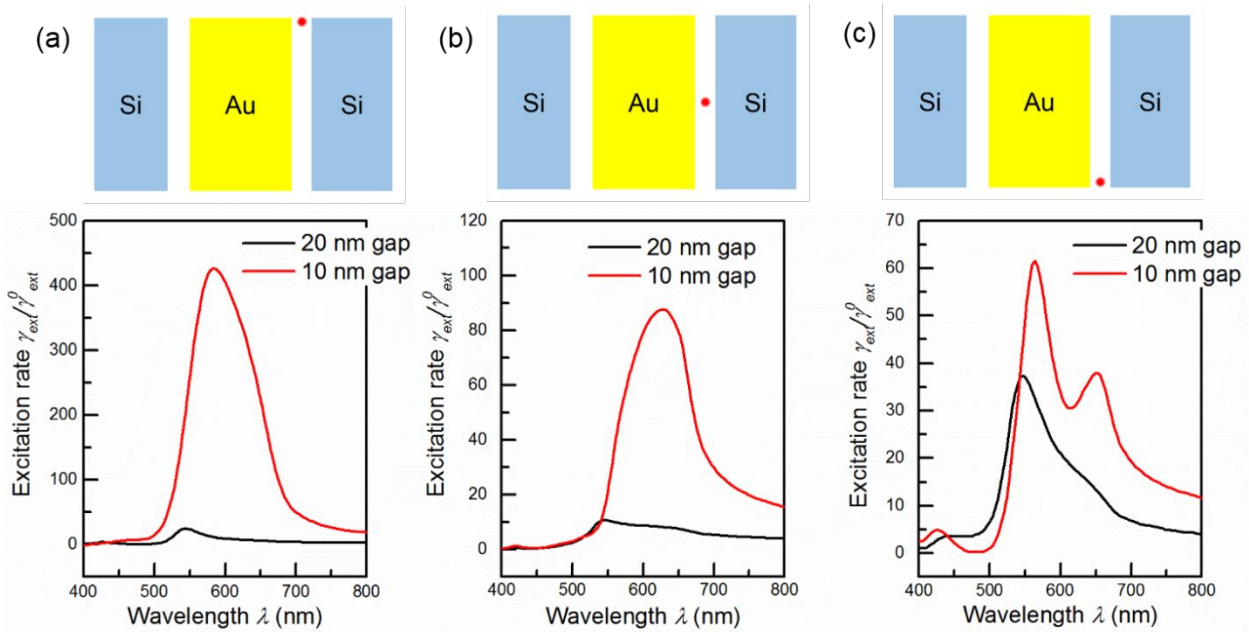

Figure S13. The excitation rates at various parts of antenna gap. Emitter is located at center of gap.

At a larger gap size, the reduced coupling strength not only reduces the excitation rates but also the radiative decay rates as shown in Figure S14. Depending on the emitter's location and

orientation, the radiative decay rates with a 20 nm gap can drop by from 10% up to a few times than that with a 10 nm gap.

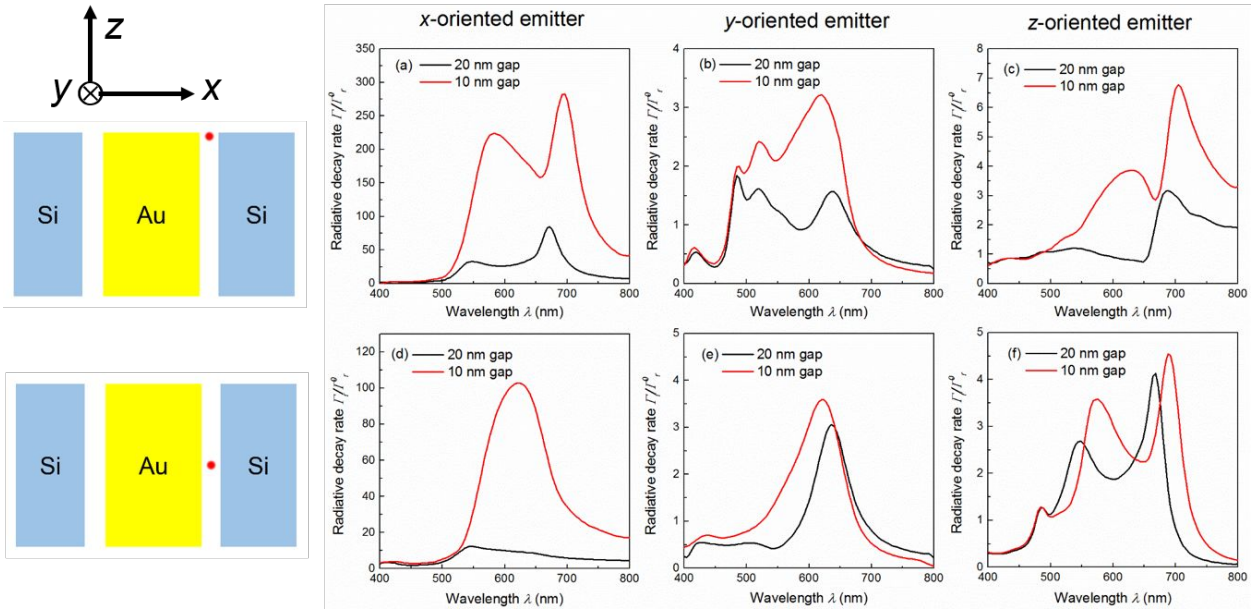

Figure S14. Radiative decay rates for various oriented emitters at different locations.

Nevertheless, a larger gap size does induces a larger quantum yield due to the suppression of the non-radiative decay loss as shown in Figure S15. With a larger gap, the emitter is relatively further away from the surface of the nanoantenna, especially the lossy metallic surface. Therefore, the non-radiative decay rate is suppressed, which leads to a higher quantum yield.

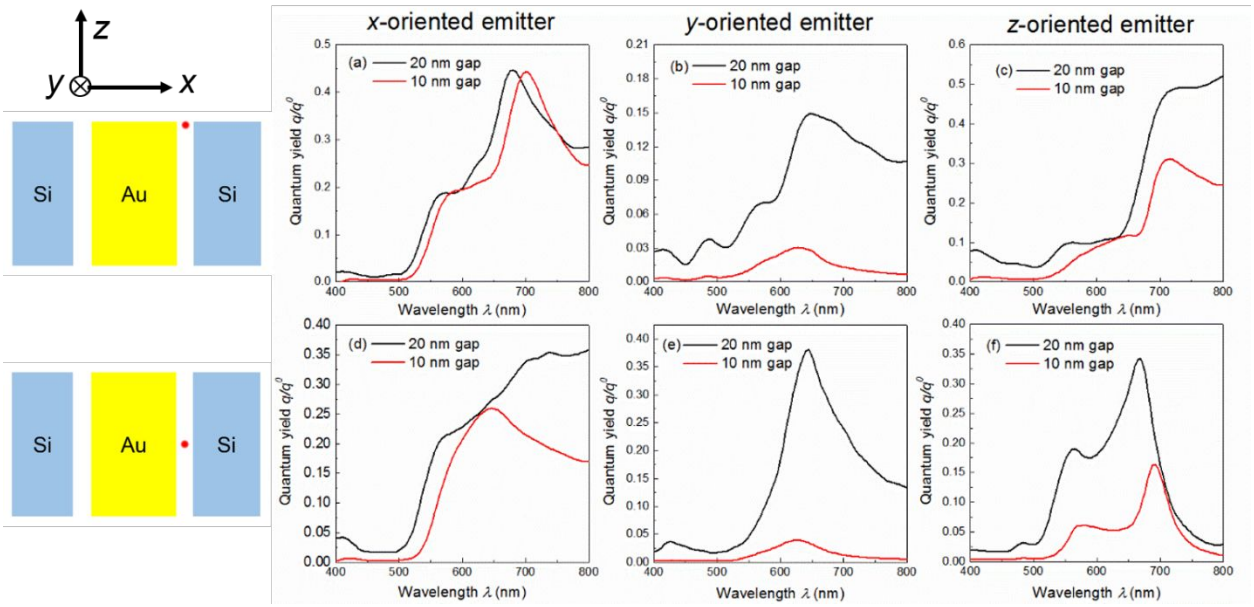

Figure S15. Quantum yields for various oriented emitters at different locations.

The resultant enhancement factor for a single emitter is shown in Figure S16. In general, the nanoantenna with a 10 nm gap can generate a larger enhancement factor than that with a 20 nm gap, owing to the larger excitation rates. Under certain condition (e.g. *y*- or *z*-oriented emitter at the top part of the gap), the relative higher quantum yield of the 20 nm gap nanoantenna could compensate the decrement in the excitation rate, and produces a comparable or even higher enhancement factor than that from a 10 nm gap nanoantenna. Nevertheless, the *x*-oriented emitters enhanced by the 10 nm gap nanoantenna have much stronger enhancement factors than the rest cases. Therefore, the 10 nm gap nanoantenna is expected to produce a larger overall fluorescence emission for multiple randomly oriented emitters than that with a 20 nm gap, which is consistent with the results in Figure 10 in the main text.

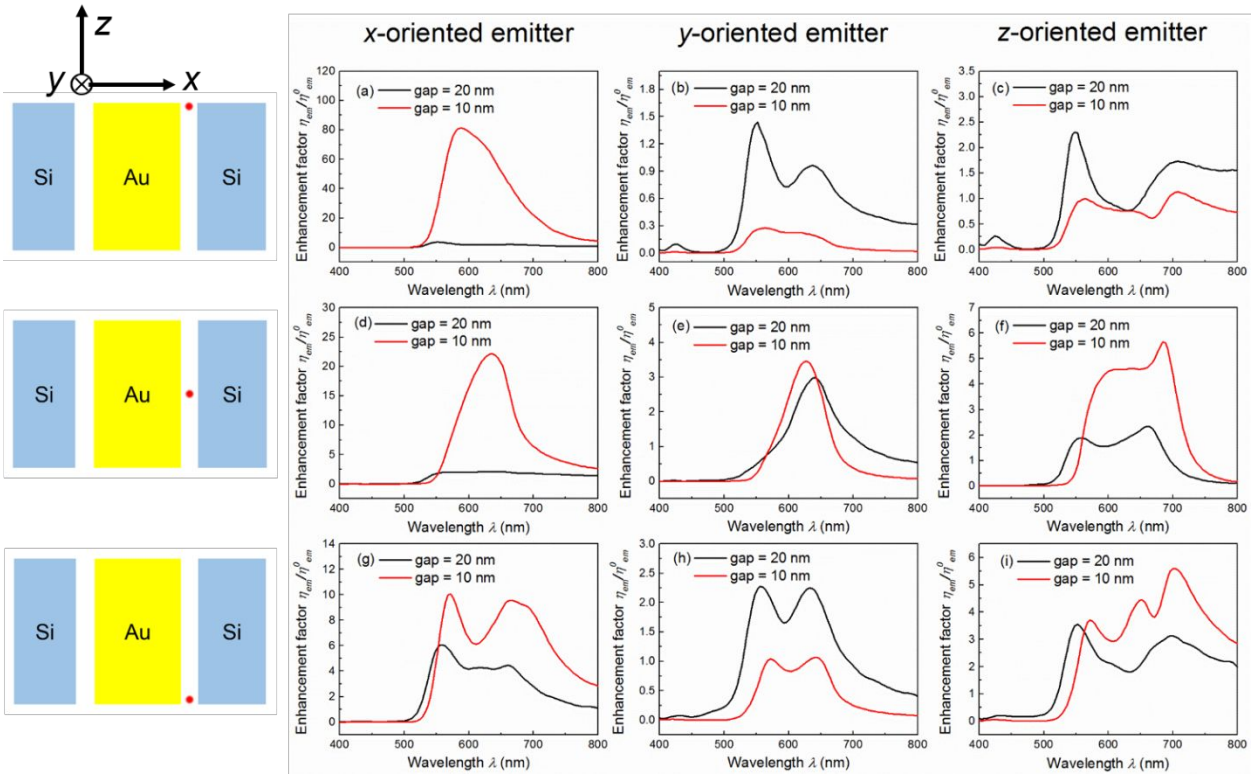

Figure S16. Enhancement factor for a single emitter with various oriented emitters at different locations.